

Coercivity limits in Nd-Fe-B hot-deformed magnets with ultrafine microstructure

N. Kulesh¹, A. Bolyachkin^{1,2}, E. Dengina^{1,3}, Xin Tang^{1,2}, T. Ohkubo¹, T. Kajiwara⁴, H. Miyawaki⁴,
H. Sepehri-Amin^{1,3*}, and K. Hono^{1,3}

¹Research Center for Magnetic and Spintronic Materials, National Institute for Materials Science,
Tsukuba 305-0047, Japan

²International Center for Young Scientists, National Institute for Materials Science, Tsukuba 305-
0047, Japan

³Faculty of Pure and Applied Sciences, University of Tsukuba, Tsukuba, 305-8573, Japan

⁴Daido Corporate Research & Development Center, Daido Steel Co., Ltd., Nakatsugawa 509-9131,
Japan

*h.sepehriamin@nims.go.jp

Abstract

In this work, we developed a series of anisotropic hot-deformed Nd-Fe-B magnets with ultrafine grain sizes varying from 125 nm to 234 nm in the lateral direction. Although grain refinement is known to increase the coercivity of magnets, all samples exhibited identical record high coercivity of 2 T. Microstructural analysis showed similar intergranular phase (IGP) composition and crystallographic texture, but increased number of coarse and isotropic equiaxed grains in the flake boundary regions of the magnets with larger grain size. Although this could explain significant differences in the initial magnetization curves and magnetic domain patterns, the experimental data alone were not enough to identify the main factors limiting the coercivity. To elucidate these, a micromagnetic simulation was performed using a realistic 1:1 scale model. We showed that the grain refinement below 200 nm has a limited potential for coercivity enhancement of hot-deformed Nd-Fe-B magnets unless the exchange interaction is weakened by reducing the magnetization of the IGP. Negative contributions to the coercivity from texture deterioration, coarse grains, and magnetostatic interaction were quantified for different values of IGP magnetization. A clear direction on how to further improve the coercivity of hot-deformed magnets was provided.

Keywords: permanent magnet; coercivity; microstructure; micromagnetic simulation

1. Introduction

High performance permanent magnets are essential components in various applications such as renewable energy generation, electric vehicles, consumer electronics, etc. To further improve energy efficiency and reduce the weight and size of devices, it is necessary to increase the energy product and optimize the extrinsic magnetic properties of the permanent magnets particularly at their operating temperatures. Although Nd-Fe-B based magnets offer the best combination of magnetization and coercivity at room temperature, their properties degrade at elevated temperatures of 150 °C and above [1]. One of the most effective ways to obtain sufficiently large coercivity at the elevated temperatures is to significantly increase the room temperature coercivity by partial substitution of Nd with heavy rare earth elements (HRE) such as Dy or Tb [2]. However, due to the scarcity and high cost of HRE, alternative ways to increase the coercivity have been explored. Grain refinement is another well-known method that has been used to increase the coercivity of sintered Nd-Fe-B magnets to ~2.0 T by reducing the grain size from 3 μm (commercial magnets) to < 1 μm (laboratory samples) [3,4]. The disadvantage of the grain refinement technology in sintered magnets is the extreme reactivity of the ultrafine $\text{Nd}_2\text{Fe}_{14}\text{B}$ powder with oxygen, which cannot be handled on an industrial scale.

Hot-deformation of melt-spun isotropic ribbons is an alternative technology for the production of high performance anisotropic Nd-Fe-B magnets [5,6]. Compared to sintered magnets, hot-deformed magnets have a much smaller grain size, which can be achieved without handling ultra-fine powders. The grain size in hot-deformed magnets can be adjusted by changing the alloy composition as well as the parameters of hot-deformation process. For example, reducing the lateral grain size from 800 nm to 210 nm resulted in a coercivity increase from 1.45 T to 1.9 T [7].

Although the increase in coercivity due to the grain refinement is a well-known experimental fact [15], it is still unclear what is the practical limit of the grain size below which there is little or no gain. The logarithmic increase in coercivity with the grain size reduction has been confirmed both experimentally [1] and by micromagnetic simulations on exchange-coupled and decoupled grains [16,17]. A simplified single-particle micromagnetic model showed that the local demagnetization field is mostly responsible for the logarithmic dependence. However, bulk magnets for practical use always have a polycrystalline microstructure, so the estimation of the stray field in a polycrystalline structure containing an intergranular phase must be incorporated into micromagnetic models for permanent magnet studies.

It should be noted that the grain shape and orientation as well as the magnetization of the intergranular phase (IGP) also have a strong influence on the coercivity and its grain size dependence [18]. The grain boundary diffusion process (GBDP) with low melting point eutectic alloys has been shown to be particularly effective in modifying the IGP. Since the eutectic diffusion process temperature is relatively low, the grain growth in the main phase is largely suppressed [8–11]. The combination of ultrafine microstructure with GBDP results in a significant increase in coercivity up to 2.5 T without the use of HRE [9]. Despite remarkable progress, the maximum coercivity value remains far below the anisotropy field of ~7 T for the $\text{Nd}_2\text{Fe}_{14}\text{B}$ phase [12–14], leaving room for further enhancement by improving the microstructure and engineering the IGP.

However, the coercivity limit with respect to the anisotropy field for a magnet with optimized microstructure is uncertain, as the previous microstructure models were too simple compared to the real microstructure of Nd-Fe-B based magnets. Considering the recent advances in the hot-extrusion that enable grain size reduction below 200 nm in the anisotropic hot-deformed Nd-Fe-B magnets [19], the effect of the grain size below the single domain size [20] must also be included in the micromagnetic simulation of the coercivity of polycrystalline magnets.

In this work, we prepared a series of hot-deformed HREE-free Nd-Fe-B magnets with different ultrafine grain sizes down to the lowest reported lateral size of 125 nm to study how microstructural features and composition of the IGP influence the hysteresis properties. Despite a twofold difference in grain size but the same alloy composition, all samples exhibited identical record high coercivity of 2 T, which is comparable to the HRE-free GBDP magnets (see benchmark in Fig. 1). To explain the observed hysteresis properties, we performed a detailed microstructural characterization and studied the magnetization reversal using static and dynamic magnetic domain analysis and magnetometry. We mainly focused on the identification of distinct microstructural features, pinning and nucleation sites, the influence of misaligned grains and intergranular phase composition on the demagnetization process. To gain a deeper insight into the mechanism of magnetization reversal, we performed micromagnetic simulations with realistic geometry based on scanning electron microscopy (SEM) images.

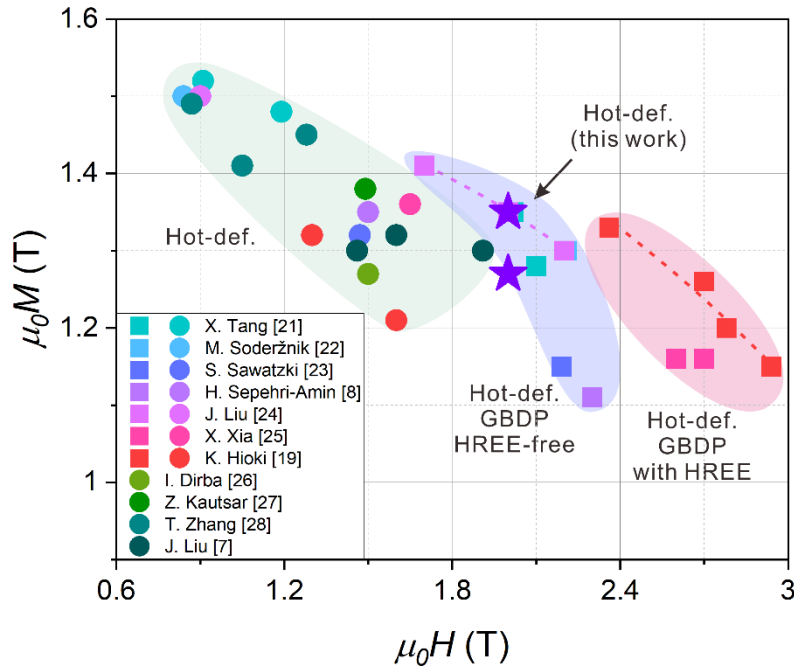


Figure 1 Coercivity vs. remanence benchmark for Nd-Fe-B hot-deformed magnets obtained without (round points) and with (rectangular points) grain boundary diffusion process [21–23,8,24,25,19,26–28,7]. The samples considered in this paper are marked with star-shaped points.

2. Samples and methods

The hot-deformed magnets with a nominal composition of $\text{Nd}_{13.5}(\text{FeCo})_{\text{bal.}}\text{Ga}_{0.57}\text{B}_{5.64}$ (at. %) were prepared by hot-press followed by hot-extrusion at the temperature range of 750-850 °C. The magnetic properties of the samples were measured by using a pulse B-H tracer and a superconducting quantum interface device vibrating sample magnetometer (SQUID-VSM). The results were corrected for the demagnetization factor based on the sample geometry. The microstructure was characterized by SEM using Carl ZEISS CrossBeam 1540EsB and by scanning transmission electron microscopy (STEM) using FEI Titan 80-300.

The magnetic domain structure was observed on polished $2 \times 2 \times 0.5$ mm samples using a magneto-optical Kerr effect (MOKE) microscope Evico Magnetics. The out-of-plane magnetization component was visualized using polar MOKE (c-axis perpendicular to the observation plane), and the in-plane magnetization component was visualized using pure longitudinal MOKE (c-axis parallel to the observation plane). In order to reduce the coercivity of the magnets to the field range reachable by the setup (1.32 T), the observation was performed at elevated temperatures up to 120 °C.

For the micromagnetic simulation, we used a 3D geometry obtained using SEM tomography data of a hot-deformed magnet, as described in detail elsewhere [29]. To reproduce the experimental grain size, we scaled the model accordingly (see section 3.4 “Micromagnetic simulation”). Geometric operations and meshing were performed using Coreform Cubit software. The micromagnetic simulation was performed using the finite element micromagnetic code “b4vex” [30], which is based on the conjugate gradient method with modified line search limited memory quasi-Newton method for energy minimization.

In the micromagnetic model, $\text{Nd}_2\text{Fe}_{14}\text{B}$ grains were assumed to have intrinsic properties of $\mu_0 M_s = 1.61$ T, $K_1 = 4.36$ MJ/m³, $A = 8$ pJ/m [31]. The thickness of the IGP separating adjacent grains was fixed at 3.5 nm. The magnetization of the IGP was varied between 0 T and 1.5 T to account for different compositions. The c-axis was oriented perpendicular to the platelet-shaped $\text{Nd}_2\text{Fe}_{14}\text{B}$ grains, which in turn were oriented according to the experimental observation by SEM and TEM results (see schematics in Fig. 2 (e-h)). The magnetic field was applied at a small angle (0.7°) of the c-axis texture to avoid artificial pinning. For the meshing, we used a tetragonal scheme with element sizes ranging from the smallest at the IGP (2.3 nm) to the largest within the $\text{Nd}_2\text{Fe}_{14}\text{B}$ grains (5.0 nm). This strategy allowed us to increase the model size (cube with a side of 800 nm) while keeping the number of elements at an acceptable level (about 170 million).

3. Results

3.1 Microstructure and magnetic properties

Due to the ultra-fine microstructure, bright field (BF)-STEM images were used to characterize the grain size of all hot-deformed magnets. For each magnet, several images were taken at different parts of the sample and automatically processed using in-house deep learning image segmentation

software. For each platelet-shaped grain detected, a tight bounding box was used to measure the lateral size, thickness, and inclination angle relative to the c-axis texture (bounding boxes with expected c-axis orientations are shown in Fig. 2 (a-d)). Statistical information on grain size distribution combined for multiple BF-STEM images is shown in Fig. 2 (e-h). The average aspect ratio of 2.8 with standard deviation (SD) of 0.8 was almost identical for all samples. The standard deviation of inclination angle $SD(\theta)$ was similar for all the samples with a tendency to increase with increasing temperature of the hot-deformation process (see the standard deviation for each sample in Fig. 2 (e-h)). Distributions of the inclination angles for each sample are shown in Fig. 1 of the Supplementary Material. Grain size analysis confirmed that the higher processing temperature leads to the more active recrystallization process, so that the larger extrusion temperature results in the larger grain size [19]. To the best of our knowledge, the ~ 125 nm grain size obtained in the anisotropic hot-deformed magnet is the finest reported so far.

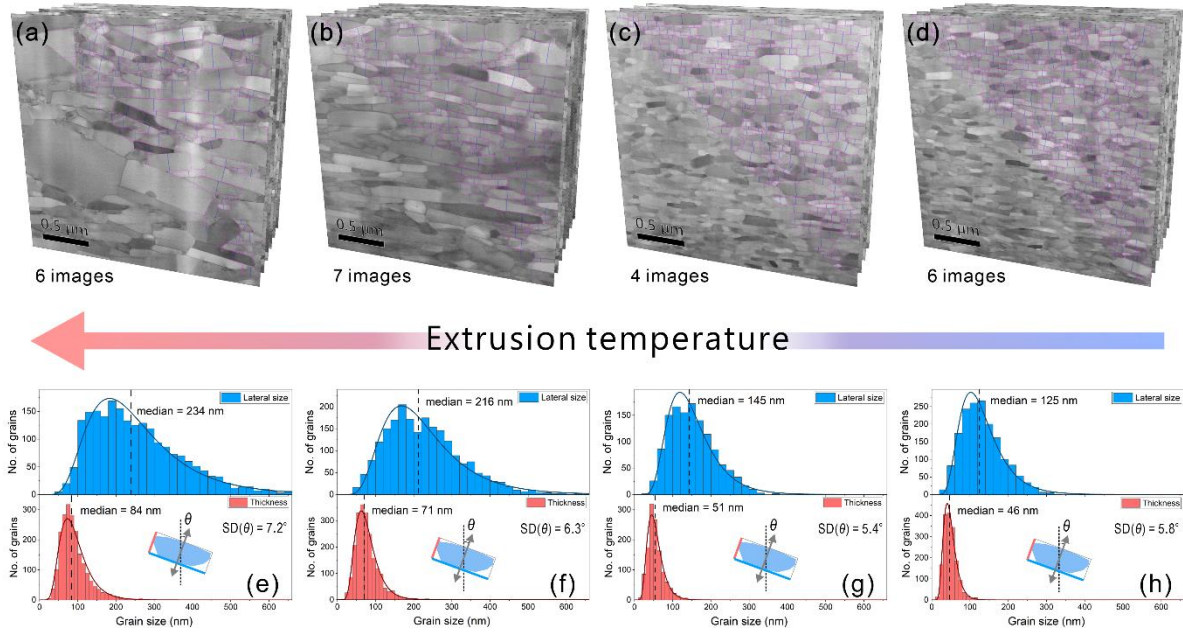


Figure 2 (a-d) BF-STEM images obtained for hot-deformed magnets produced with different extrusion temperatures. In the upper right corner of each image an example of automatic processing is shown: tight bounding boxes for each detected grain (magenta lines) and estimated orientations of the c-axis (blue lines). (e-h) Results of the statistical analysis performed for each series of images (the number of images used for the analysis is indicated at the bottom of each TEM image a-d). The standard deviations of inclination angle $SD(\theta)$ are shown in the bottom section of each histogram.

The collected statistics show that the four studied samples can be divided into two pairs with distinctly different grain sizes and sharpness of the grain size distributions: (e, f) and (g, h) in Fig. 2. The initial magnetization and demagnetization curves measured for all four samples (see Fig. 3 (a)) confirm the similarity of the two samples with smaller (145 nm and 125 nm lateral size) and two samples with larger (216 nm and 234 nm lateral size) grain size. The first stage of the initial magnetization curves shows relatively large susceptibility for samples with an average grain size of 216 nm and 234 nm and smaller susceptibility for the samples with smaller grain sizes of 145 nm

and 125 nm in lateral direction. Initial large susceptibility corresponds to easy domain wall displacement within the multi-domain grains, and the change in susceptibility in the initial magnetization curve corresponds to the domain wall displacement through the intergranular phase. Note that the so-called depinning field, corresponding to the magnetic field at which the concavity of the initial magnetization curve changes from negative to positive value, is identical for all samples (1.85 T).

Although all samples show comparable saturation magnetization due to the same alloy composition, the remanent magnetization decreases with increasing in the extrusion temperature. It is interesting to note that there is a clear correlation between the measured $SD(\theta)$ values and the remanence. For example, the smallest value of 5.4° corresponds to the sample with the second smallest grain size of 145 nm, which shows the highest remanence. For further in-depth analysis, we selected the samples with the largest and the smallest average grain sizes (LG and SG respectively), which show the most difference in microstructure as well as initial magnetization and demagnetization curves.

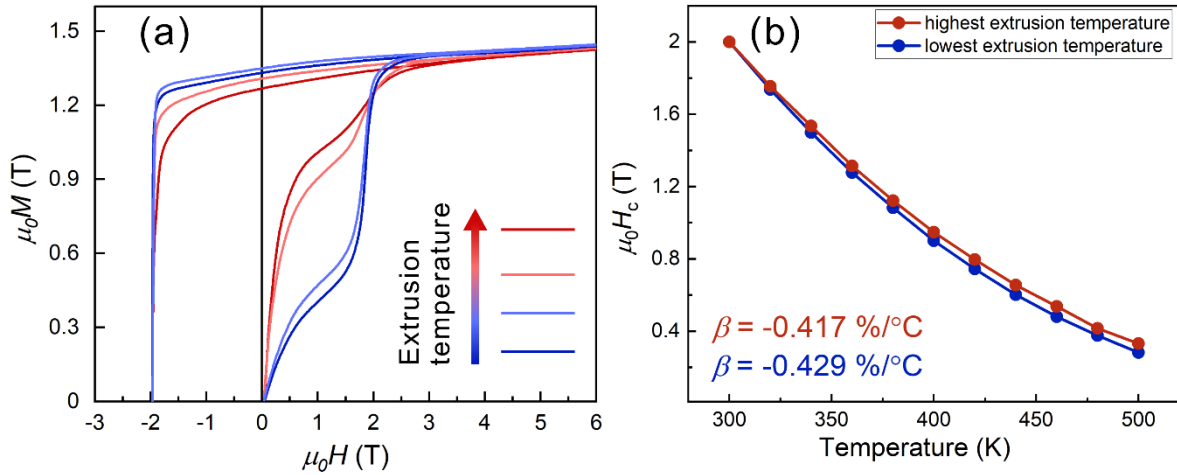


Figure 3 (a) Initial magnetization and demagnetization curves measured on samples with different extrusion temperature. (b) Temperature dependencies of coercivities measured on samples with the smallest grain size of 125 nm (blue dots) and maximum grain size of 234 nm (red dots).

Temperature coefficients for coercivity are shown in the inset with corresponding colors.

The coercivity values $\mu_0 H_c$ measured for the two samples at elevated temperature in Fig. 3 (b) start to diverge, showing an overall better stability for the SG sample, but the difference remains marginal. The temperature coefficients of coercivity calculated for the 300 – 500 K range also have similar values: $\beta = -0.417 \text{ \%}/\text{K}$ for the LG sample and $\beta = -0.429 \text{ \%}/\text{K}$ for the SG sample.

To compare the effect of the microstructure of different magnets on the coercivity, the Kronmüller equation can be used: $H_c = \alpha H_A - N_{eff} M_s$, where $H_A = 2K_u/(\mu_0 M_s)$ is the anisotropy field [32]. Here H_c is the coercivity, K_u is the uniaxial magnetocrystalline anisotropy constant, M_s – spontaneous magnetization, α is the combined parameter responsible for the coercivity reduction due to the grain misalignment and reduced anisotropy at the grain surface, and N_{eff} is the effective demagnetization factor including contributions from the shape of the magnet, the arrangement and shape of the grains, and the shape of the nucleation sites. $H_c(T)/M_s(T)$ versus $H_A(T)/M_s(T)$ plots

(see Fig. 2 in the Supplementary Material) were used to estimate α (slope) and N_{eff} (extrapolation of the linear region). As a result, similar values of the α and N_{eff} parameters were obtained for magnets with different grain sizes (see Table 1). The values of the α parameter for both samples are typical for a nanocrystalline Nd-Fe-B magnet [33,34].

Table 1 Average values of the microstructural parameters estimated for finite element models used for micromagnetic simulation. Models with the largest and smallest grain sizes correspond to the LG and SG samples respectively.

Sample	Kronmüller plot		Nd+Pr concentration in IGP (at.%)	
	α	N_{eff}	c-plane	side-plane
Largest grains	0.67	1.17	39 ± 9	34 ± 10
Smallest grains	0.63	1.32	41 ± 3	30 ± 5

Low magnification backscattered electron (BSE) SEM images for the LG and SG samples are shown in Fig. 4. The SG sample has a thin and well-localized Nd-rich interface between melt-spun flakes with few large Nd-O inclusions visible in Fig. 4 (a). On the contrary, the LG sample has relatively thick and irregular Nd-rich flake boundaries, visible in Fig. 4 (b), filled with large equiaxed grains $\text{Nd}_2\text{Fe}_{14}\text{B}$ grains, clearly observed in Fig. 4 (d). The microstructure is consistent with the magnetometry data in Fig. 3 (a) and can explain the reduced remanence and increased initial susceptibility of the samples with higher extrusion temperature.

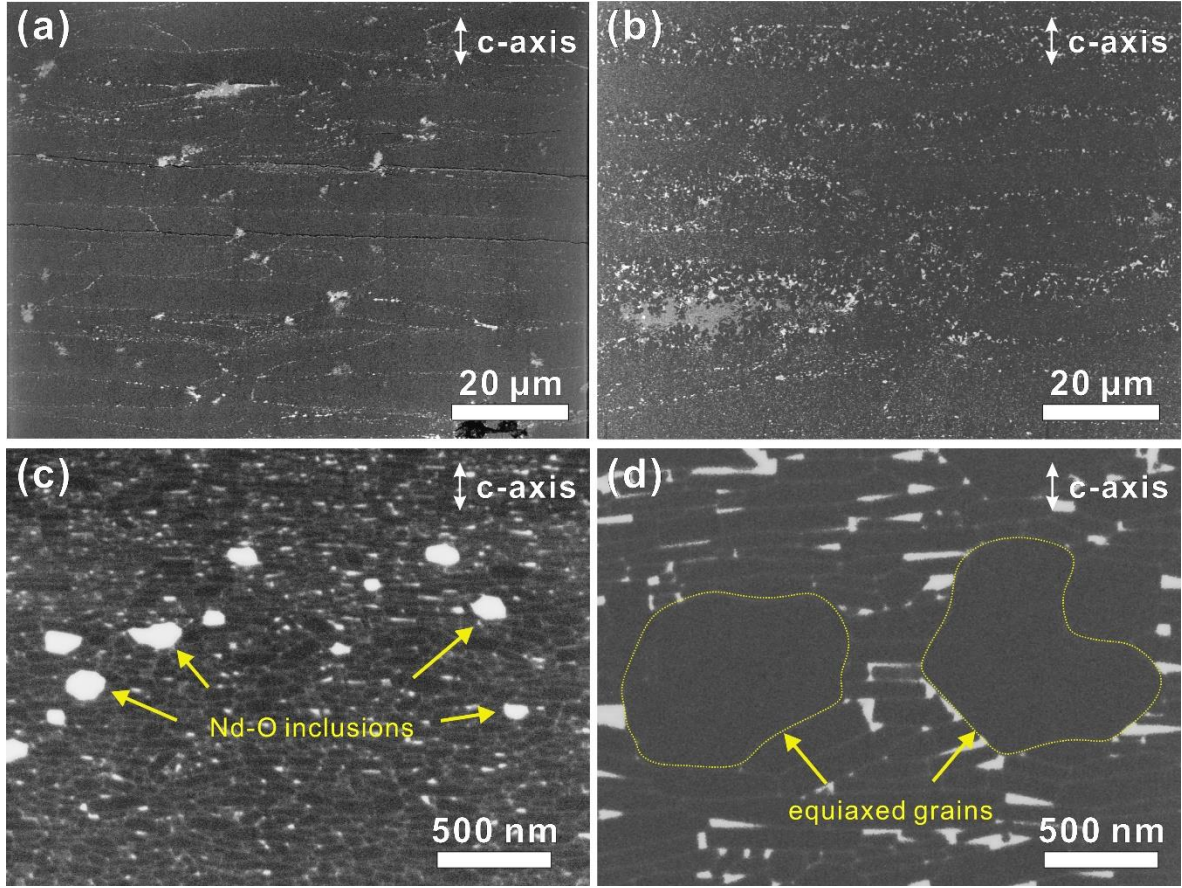


Figure 4 BSE-SEM images obtained for samples of hot-deformed magnets with lowest (a, c) and highest (b, d) extrusion temperature at different magnifications.

High magnification HAADF-STEM images, superimposed STEM-EDS maps across the IGP, and composition line profiles obtained from STEM-EDS results for SG and LG samples are shown in Fig. 5. To have a better statistic of the IGP composition in each hot-deformed magnet, the composition of 7 to 10 IGP was analyzed by STEM-EDS for each sample. The average concentration of Nd+Pr in the IGP of the SG sample was 37 at.%, which is very similar to 36 at.% measured for the LHE sample. The difference between the concentrations of rare-earth elements in IGPs parallel to the c-plane and side plane for both samples was 5-10 at.%. The RE concentrations in IGPs of LG and SM samples are summarized in Table 1. More examples of the collected compositional profile are shown in Fig. 3 of the Supplementary Material.

Although IGP is known to be ferromagnetic in Nd-Fe-B magnets, the reported magnetization values vary widely depending on the sample and the methodology. For example, the experimentally measured magnetization of IGP ($\mu_0 M_{IGP}$) in sintered magnets varies from 0.55 to 1.0 T [35,36], while values defined by the first-principle calculation are between 1.0 and 1.15 T for Nd content of 42 – 54 at.% [14]. Therefore, it can be concluded that the intergranular phase with ~64 at. % Fe is ferromagnetic. Despite significant uncertainties in the absolute value of its magnetization [14, 34, 35], similar chemical compositions of the IGP in SG and LG samples indicate comparable $\mu_0 M_{IGP}$.

values. The compositional profiles for both samples also show 3.5 ± 1.5 at.% Ga localized in the IGP, which is known to improve the wettability of the intergranular phase and may slightly reduce the $\mu_0 M_{IGP}$ [37]. The typical IGP thickness far from the triple junctions was found to be about 2-3 nm.

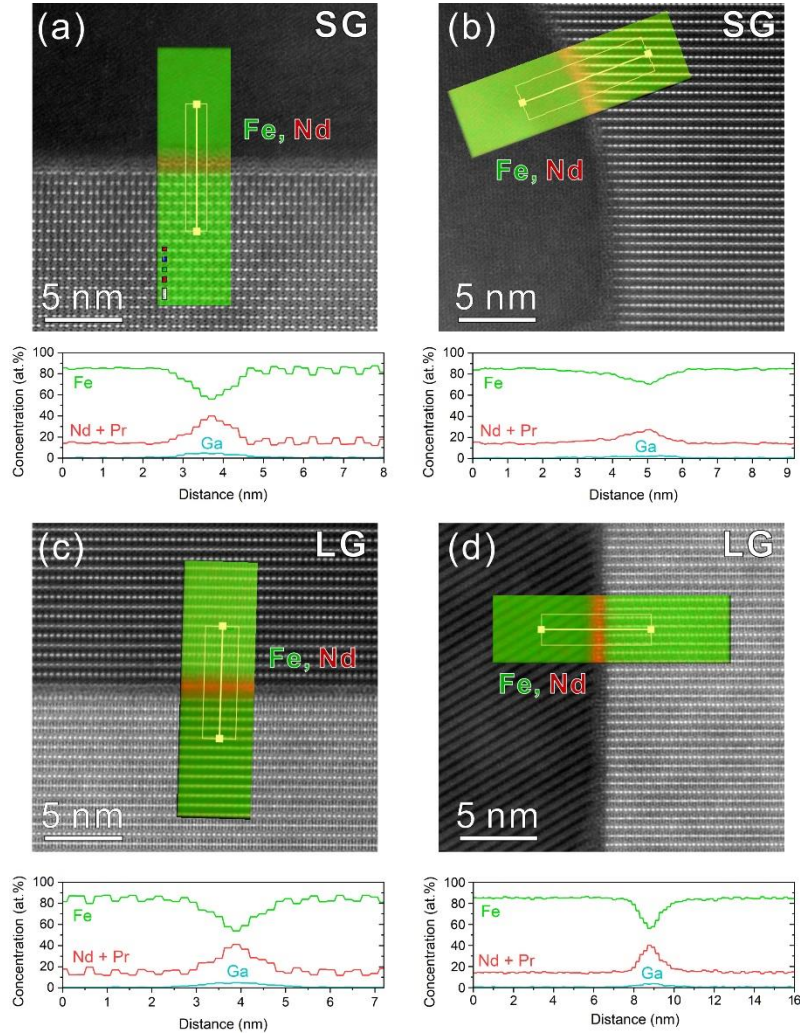


Figure 5 High magnification HAADF-STEM images with STEM-EDS map for hot-deformed samples with smallest (a,b) and largest (c,d) grain size obtained for IGP parallel (a,c) and perpendicular (b,d) to c-axis. The averaged composition line profile across the IGP region is shown in the lower part of each corresponding HAADF-STEM image.

3.3 Magnetic domains analysis with MOKE microscopy

Fig. 6 (a, b, d, e) shows the magnetic domain structure of thermally demagnetized SG and LG samples visualized by MOKE microscopy without applying an external magnetic field. The polar mode observation for the SG sample shows a fine labyrinth domain pattern, mostly uninterrupted by thin melt-spun flake boundaries. Thicker interface regions in the LG sample lead to the disappearance or disruption of the domain pattern, as shown in Fig. 6 (d). A similar tendency continues for the domain pattern observed parallel to the c-axis. The domain pattern for the SG sample shown in Fig. 6 (b) consists of continuous stripes passing through the interface of melt-spun flakes. In contrast, thicker interfaces, as seen in Fig. 6 (e) for the LG sample, cause disruption and brunching of the stripe-like domain pattern. Local disruption of the domain wall in the interface region is also evident from the Lorentz transmission electron microscopy images in Fresnel mode shown in Fig. 6 (c, f). Note that the magnetic domain walls in the Fresnel images with bright and dark contrasts are marked with white arrows, while the original flake boundaries are marked with yellow arrows. The thin interface of the SG sample contains relatively few scattered defects, whereas the thick interface of the LG sample consists of many large multidomain grains with highly misaligned c-axis.

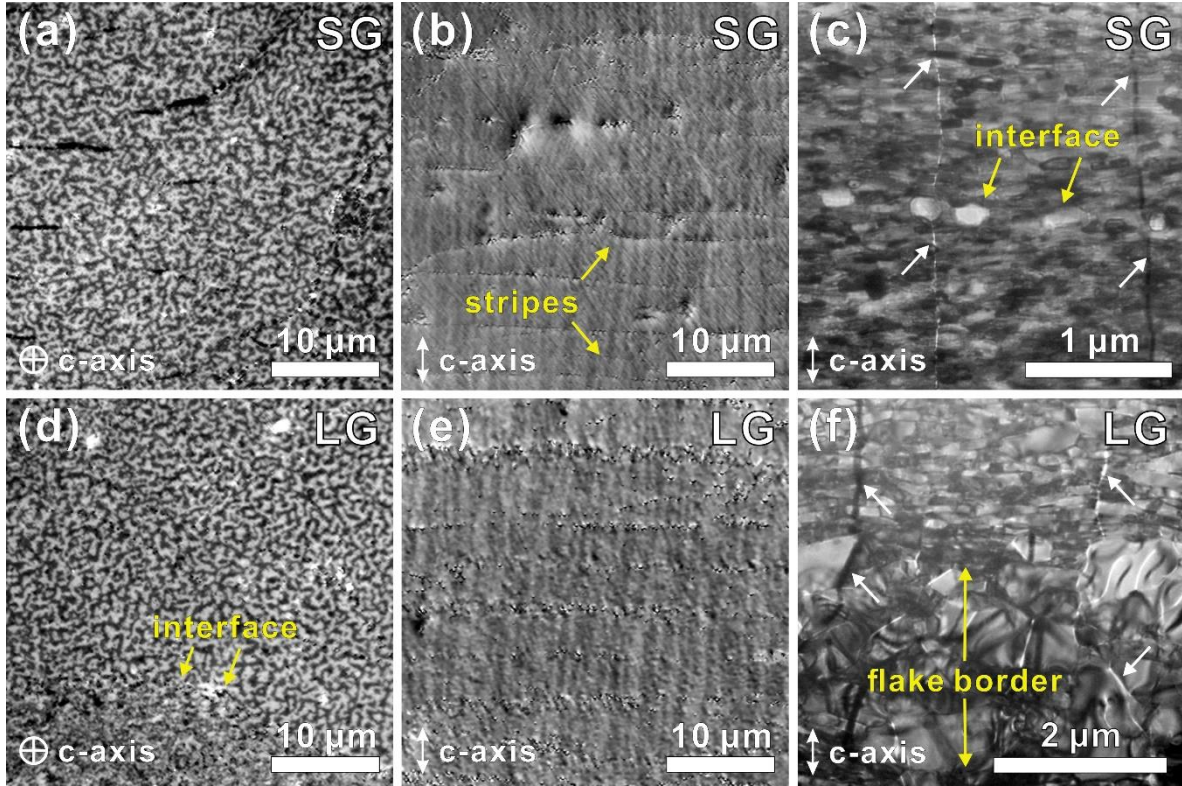


Figure 6 MOKE microscopy images obtained on SG (a, b) and LG (d, e) samples of hot-deformed magnets in the thermally demagnetized state. Maze-like domains (a, d) are obtained in polar mode, stripe-like domains parallel to the c-axis (b, e) are visualized in longitudinal mode. Lorentz transmission microscopy images near the melt-spun flake interface (indicated by yellow arrows) for SG (c) and LG (f) samples. White arrows indicate the position of domain walls near the interface.

The maximum amplitude of the magnetic field available in the MOKE microscope was 1.32 T, which is far below the coercive field of the samples studied. To obtain the remanence state, we used an external 5 T pulsed magnetic field source to fully magnetize the samples. After the magnets were placed in the measurement system, they were heated up to reduce the coercivity. Fig. 7 shows selected magnetic domain patterns obtained for SG and LG samples along the c-axis while gradually increasing the amplitude of the applied reverse magnetic field. For both samples, magnetization reversal begins in the interface of melt-spun flakes containing large equiaxed grains. For the LG sample, individual reversal sites appear at relatively low fields around 0.4 T, while for the SG sample nucleation sites become visible only at 1.1 T. For both samples, the domain wall starts to propagate only at a magnetic field close to the coercivity and shows a preferential direction perpendicular to the boundaries of the original melt-spun flakes. Although the maximum magnetic field and temperature available in our setup were not sufficient to completely reverse the magnetization in the SG sample, we could observe how the magnetization reversal initiates and propagates. Investigation of the magnetization reversal in the polar MOKE mode confirmed the presence of many equiaxed grains in the thick interface region of the LG sample (see Fig. 4 in the Supplementary Material), which were not present in the SG sample.

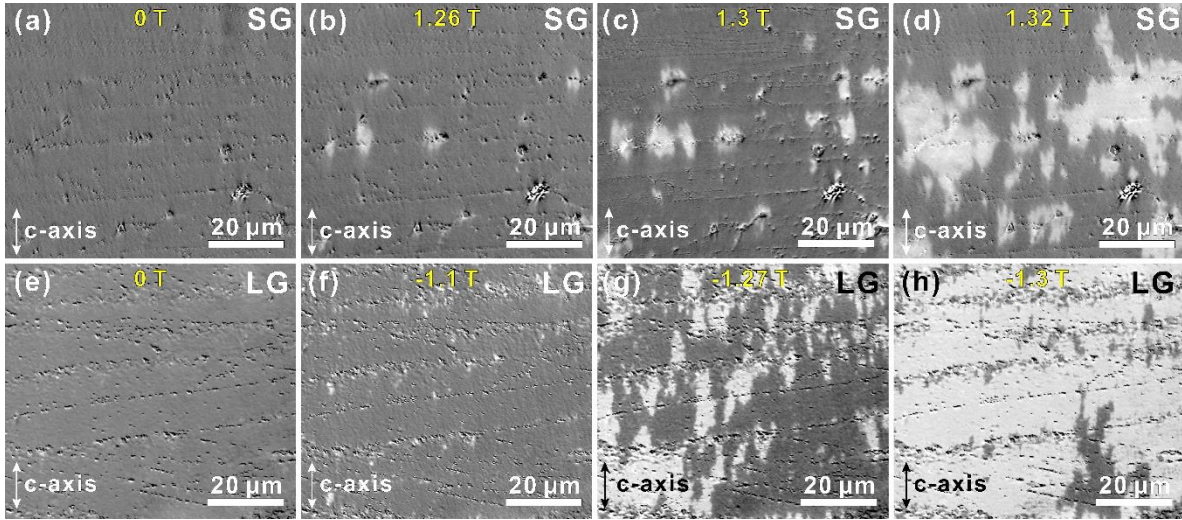


Figure 7 Sequential MOKE microscopy images obtained by applying opposite magnetic field (value is indicated in yellow font) along the c-axis on SG (a-d) and LG (e-h) samples of hot-deformed magnets at elevated temperature $T = 390$ K (SG sample) and $T = 370$ K (LG sample).

3.4 Micromagnetic simulation

To analyze the magnetization reversal in hot-deformed samples with different grain size and intergranular phase magnetization, we used micromagnetic simulation with realistic tomography-based geometry [38]. The geometry was scaled to reproduce the experimental distribution obtained from the segmented TEM images of the LG and SG samples (Fig. 2 (e, h)). To ensure consistency with the experimental data, the average grain size, aspect ratio, and tilt angle for the model were measured in a similar manner: four slices were taken from the model geometry and processed with

the same algorithm used for the automatically segmented experimental images. The total number of grains was varied from 98 for the model with the larger grains to 518 for a model with the smallest grain size. The final geometries for the lateral grain sizes of 250 nm and 155 nm with reconstructed IGP are shown in Fig. 8 (a, b). The average grain sizes, aspect ratios, and tilt angles for all finite element models are summarized in Table 2.

Table 2 Average values of the microstructural parameters estimated for finite element models used for micromagnetic simulation. Models with the largest and smallest grain sizes correspond to the LG and SG samples respectively.

Model	Lateral grain size (nm)	Grain thickness (nm)	Aspect ratio	SD of EA inclination angle (°)
Largest grain size	250 ± 122	84 ± 45		
Intermediate grain size	200 ± 100	67 ± 36	2.9 ± 0.9	7.6
	155 ± 60	50 ± 22		
Smallest grain size	125 ± 48	40 ± 18		

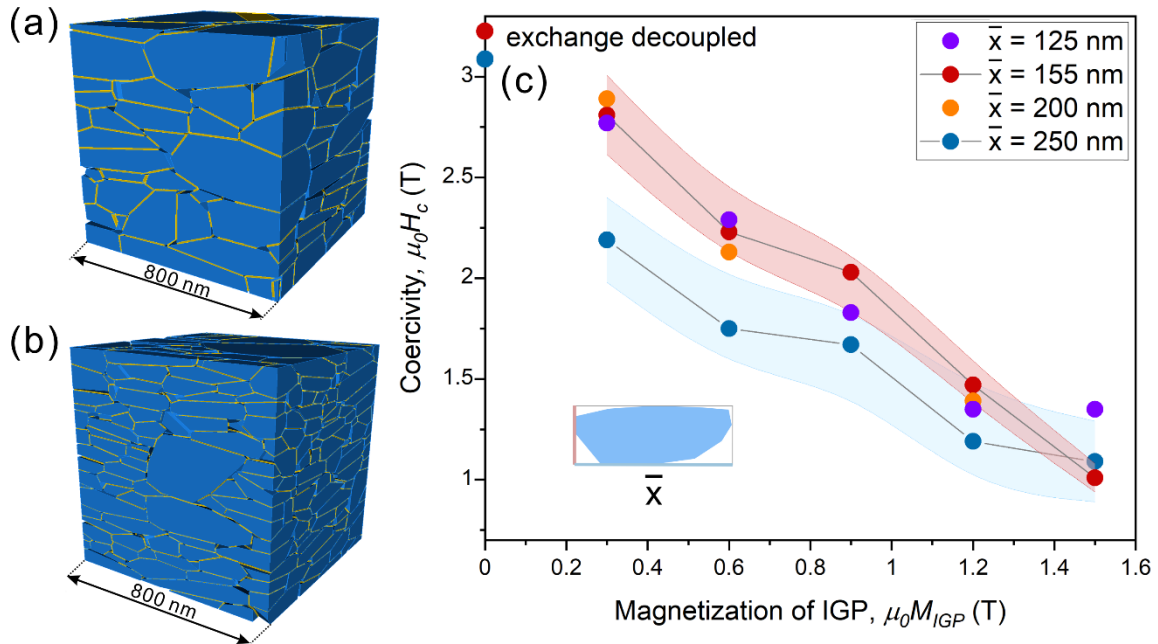


Figure 8 The tomography-based geometries constructed for the micromagnetic simulation with mean lateral grain sizes of 250 nm (a) and 155 nm (b) corresponding to the LG and SG samples, respectively. IGP are shown in yellow, nonmagnetic triple junctions are set invisible. Coercivity dependence on IGP magnetization simulated for samples with different mean lateral grain size (\bar{x}) and thickness (\bar{y}) (c).

To mimic the presence of equiaxed grains near the flake boundaries, the easy magnetization axis was rotated by 70° relative to the c-axis for the large grains near the cube face, while keeping the magnetization, magnetic anisotropy constant, and exchange constant the same. The dependencies of the coercivity on the IGP magnetization simulated for models with different grain sizes are shown in Fig. 8 (c). To estimate the uncertainty interval, we performed simulations for five different models with the largest grain size (shown with light blue area in Fig. 8 (c)). The micromagnetic simulation results show that the smaller grain size leads to a significant coercivity enhancement only when the magnetization of the IGP is relatively low.

4. Discussion

The microstructural analysis of SG and LG hot-deformed magnets showed an almost 2 times larger grain size for the LG sample and a distinctly different flake boundary region with numerous coarse equiaxed grains for the LG and relatively small and sparse equiaxed grains for the SG sample. According to the results of STEM-EDS analysis, the IGP is ferromagnetic with magnetization roughly estimated to be between 0.4 and 0.9 T. The microstructural analysis and MOKE microscopy showed that equiaxed grains which are isotropic in broad flake boundaries in the LG sample as well as larger platelet misalignment are responsible for the reduced remanence in Fig. 3 (a), but the process of magnetization reversal is similar for SG and LG samples and starts at the flake boundary region regardless of the different volume fraction of large equiaxed grains. The cascade propagation of the domain wall into the flakes is almost identical for both samples, suggesting an identical depinning field at the IGP, which is also found in the initial magnetization curves.

The micromagnetic simulation for coarse and fine microstructure models showed a comparable coercivity when $\mu_0 M_{IGP} > 0.9$ T (Fig. 8(c)). In other words, a larger coercivity in the smaller grain size magnets can only be obtained by separating the $\text{Nd}_2\text{Fe}_{14}\text{B}$ grains with a weakly ferromagnetic IGP. A deeper understanding of the coercivity in hot-deformed magnets requires consideration of the individual contributions of the microstructural parameters, i.e., grain size, grain misalignment, equiaxed grains, and magnetization of the IGP. We performed a series of simulations for the models with smaller and larger grain sizes, in which we sequentially included the contributions of the demagnetization field, easy axis misalignment, and equiaxed grains (easy magnetization axis is rotated 70° relative to the texture axis, mimicking the presence of equiaxed grains in the flake boundaries). Since we do not have a reliable information on the magnetization of the IGP, each round of the simulation was run for different $\mu_0 M_{IGP}$ values, starting from 0.0 T, which corresponds to the case of exchange decoupled grains. The coercivity reduction after adding each contribution for small and large grain size models with different values of $\mu_0 M_{IGP}$ is summarized in the Fig. 9 (b, c). The maximum coercivity $\mu_0 H_c = 6.17$ T obtained for both models is lower than the anisotropy field for $\text{Nd}_2\text{Fe}_{14}\text{B}$ $\mu_0 H_A \approx 6.85$ T due to the orientation of the external field under the small angle with respect to the anisotropy axis (0.7°).

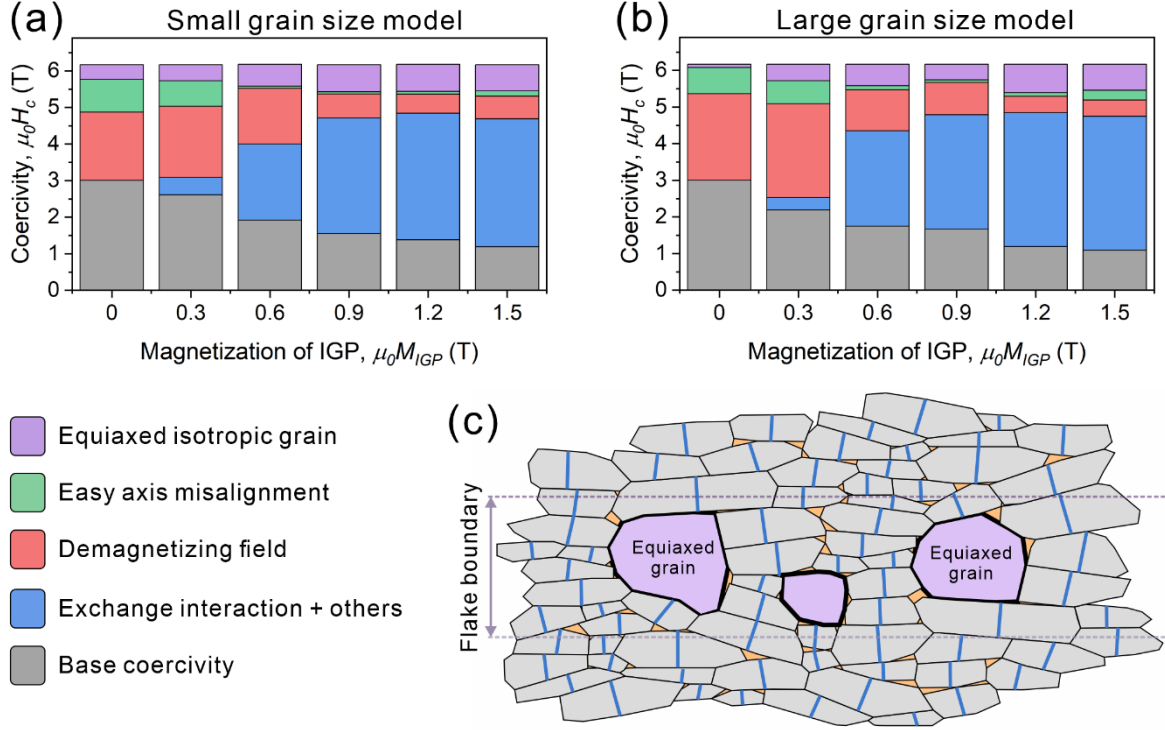


Figure 9 Main contributions to the coercivity reduction estimated with micromagnetic simulation for magnets with smaller (a) and larger (b) grain sizes. Legend with color codes is shown in the bottom left side. Schematic showing considered microstructural defects: grain misalignment relative to c-axis texture (local easy axes are shown with blue lines) and equiaxed grain (in the flake boundary region) (c).

The analysis of the negative contributions to the coercivity shows the dominance of the exchange interaction for $\mu_0 M_{IGP} \geq 0.6$ T, which also leads to the reduced effect of large equiaxed grains (see Fig. 9 (c)). In this regime, the effect of smaller grain size in increasing the coercivity becomes negligible due to the stronger overall negative effect of the exchange interaction, which can explain the identical coercivities observed experimentally. Grain refinement is the most beneficial for $\mu_0 M_{IGP} \leq 0.6$ T due to the reduced contribution of the demagnetization field, which is consistent with the previously reported logarithmic decay of the demagnetization factor for smaller grain size [18]. Thus, for the grain refinement to be effective in increasing the coercivity, the magnetization of M_{IGP} should be reduced accordingly as realized by our micromagnetic simulations (Fig. 8(c)).

Since the experimental results and micromagnetic simulations show a limited potential of grain refinement for further coercivity enhancement in the exchange-coupled hot-deformed magnets, the question arises as to what further improvements can be made to enhance hard magnetic properties of hot-deformed magnets. Based on the simulation results, we can estimate the potential of several alternative paths:

- *Elimination of large equiaxed grains.* Micromagnetic simulation performed on the models with different grain sizes without misoriented grains showed 0.2 – 0.5 T coercivity improvement over the same range of $\mu_0 M_{IGP}$ as shown in Fig. 9 (b,d). However, the

experimental characterization of the SG and LG samples with very different densities of large equiaxed grains showed no coercivity difference. This means that even a small number of equiaxed grains may be sufficient to initiate nucleation if M_{IGP} is relatively high [39].

- *Reduction of the easy axis misalignment.* The angle of misalignment is known to be one of the most important factors in reducing the coercivity of permanent magnets [40]. However, for the ultrafine grain samples in this work, the $SD(\theta)$ was measured to be 5.7° , which is already a relatively low value. Further improvement of the coercivity is possible, but largely limited by the process engineering. The estimated coercivity gain can reach $0.5 - 0.9$ T when $\mu_0 M_{IGP} \leq 0.3$ T.
- *Reduction of IGP magnetization.* This method remains the most promising. Micromagnetic simulation on a fully decoupled model (nearly zero $\mu_0 M_{IGP}$) shows that the coercivity of the considered samples can potentially reach 3.1 T. Hence, further optimization of IGP composition by both alloy design and post-treatments such as eutectic grain boundary diffusion process could be the solution.

5. Conclusion

In this paper, we have investigated how microstructural parameters define coercivity and magnetization reversal in anisotropic Nd-Fe-B based hot-deformed magnets with the same alloy composition and identical 2.0 T coercivity despite twofold difference in grain size. Detailed microstructural analysis and MOKE microscopy have shown that the magnetization reversal starts at the flake boundary region for both fine and coarse microstructure samples. This suggests that for ultrafine grain size samples, the magnetization reversal is mainly controlled by the pinning of magnetic domain walls inside the flakes, i.e. at the intergranular phase.

The identical coercivity for different grain sizes was interpreted with the micromagnetic simulation based on SEM tomography data, which allowed us to evaluate the contributions of microstructural parameters to the coercivity separately. These results confirmed that the grain refinement has a limited potential for further coercivity enhancement due to the increased contribution of the exchange interaction when the magnetization of the intergranular phase is larger than 0.6 T, which is the case for all commercially available hot-deformed magnets. In the intermediate range of $0.3 \text{ T} \leq \mu_0 M_{IGP} \leq 0.6 \text{ T}$, very similar coercivity is expected regardless of the grain size. Based on the analysis results, recommendations for further improvement of the coercivity were proposed. We believe that this work will contribute to the further development of high performance Nd-Fe-B permanent magnets.

References

- [1] K. Hono, H. Sepehri-Amin, Strategy for high-coercivity Nd-Fe-B magnets, Scripta Materialia. 67 (2012) 530–535. <https://doi.org/10.1016/j.scriptamat.2012.06.038>.
- [2] S. Hirosawa, K. Tokuhara, Y. Matsuura, H. Yamamoto, S. Fujimura, M. Sagawa, The dependence of coercivity on anisotropy field in sintered R-Fe-B permanent magnets, Journal

- of Magnetism and Magnetic Materials. 61 (1986) 363–369. [https://doi.org/10.1016/0304-8853\(86\)90050-8](https://doi.org/10.1016/0304-8853(86)90050-8).
- [3] H. Sepehri-Amin, Y. Une, T. Ohkubo, K. Hono, M. Sagawa, Microstructure of fine-grained Nd–Fe–B sintered magnets with high coercivity, *Scripta Materialia*. 65 (2011) 396–399. <https://doi.org/10.1016/j.scriptamat.2011.05.006>.
 - [4] Y. Une, M. Sagawa, in: *The 21st Workshop on Rare-Earth Permanent Magnets and Their Applications*, Bled, Slovenia, 2010.
 - [5] J.J. Croat, J.F. Herbst, R.W. Lee, F.E. Pinkerton, Pr-Fe and Nd-Fe-based materials: A new class of high-performance permanent magnets (invited), *Journal of Applied Physics*. 55 (1984) 2078–2082. <https://doi.org/10.1063/1.333571>.
 - [6] R.W. Lee, Hot-pressed neodymium-iron-boron magnets, *Appl. Phys. Lett.* 46 (1985) 790–791. <https://doi.org/10.1063/1.95884>.
 - [7] J. Liu, H. Sepehri-Amin, T. Ohkubo, K. Hioki, A. Hattori, T. Schrefl, K. Hono, Grain size dependence of coercivity of hot-deformed Nd–Fe–B anisotropic magnets, *Acta Materialia*. 82 (2015) 336–343. <https://doi.org/10.1016/j.actamat.2014.09.021>.
 - [8] H. Sepehri-Amin, T. Ohkubo, S. Nagashima, M. Yano, T. Shoji, A. Kato, T. Schrefl, K. Hono, High-coercivity ultrafine-grained anisotropic Nd–Fe–B magnets processed by hot deformation and the Nd–Cu grain boundary diffusion process, *Acta Materialia*. 61 (2013) 6622–6634. <https://doi.org/10.1016/j.actamat.2013.07.049>.
 - [9] H. Sepehri-Amin, L. Liu, T. Ohkubo, M. Yano, T. Shoji, A. Kato, T. Schrefl, K. Hono, Microstructure and temperature dependent of coercivity of hot-deformed Nd–Fe–B magnets diffusion processed with Pr–Cu alloy, *Acta Materialia*. 99 (2015) 297–306. <https://doi.org/10.1016/j.actamat.2015.08.013>.
 - [10] T. Akiya, J. Liu, H. Sepehri-Amin, T. Ohkubo, K. Hioki, A. Hattori, K. Hono, High-coercivity hot-deformed Nd–Fe–B permanent magnets processed by Nd–Cu eutectic diffusion under expansion constraint, *Scripta Materialia*. 81 (2014) 48–51. <https://doi.org/10.1016/j.scriptamat.2014.03.002>.
 - [11] Z. Liu, J. He, R.V. Ramanujan, Significant progress of grain boundary diffusion process for cost-effective rare earth permanent magnets: A review, *Materials & Design*. 209 (2021) 110004. <https://doi.org/10.1016/j.matdes.2021.110004>.
 - [12] J.F. Herbst, R 2 Fe 14 B materials: Intrinsic properties and technological aspects, *Rev. Mod. Phys.* 63 (1991) 819–898. <https://doi.org/10.1103/RevModPhys.63.819>.
 - [13] J. Li, H. Sepehri-Amin, T. Ohkubo, K. Hono, Identifying the mechanism of hard magnet coercivity by its angular dependence, *Phys. Rev. B*. 105 (2022) 174432. <https://doi.org/10.1103/PhysRevB.105.174432>.
 - [14] X. Tang, J. Li, H. Sepehri-Amin, A. Bolyachkin, A. Martin-Cid, S. Kobayashi, Y. Kotani, M. Suzuki, A. Terasawa, Y. Gohda, T. Ohkubo, T. Nakamura, K. Hono, Unveiling the origin of the large coercivity in (Nd, Dy)-Fe-B sintered magnets, *NPG Asia Mater.* 15 (2023) 50. <https://doi.org/10.1038/s41427-023-00498-5>.
 - [15] R. Ramesh, K. Srikrishna, Magnetization reversal in nucleation controlled magnets. I. Theory, *Journal of Applied Physics*. 64 (1988) 6406–6415. <https://doi.org/10.1063/1.342054>.
 - [16] J. Fischbacher, A. Kovacs, M. Gusenbauer, H. Oezelt, L. Exl, S. Bance, T. Schrefl, Micromagnetics of rare-earth efficient permanent magnets, *J. Phys. D: Appl. Phys.* 51 (2018) 193002. <https://doi.org/10.1088/1361-6463/aab7d1>.
 - [17] H. Sepehri-Amin, T. Ohkubo, M. Gruber, T. Schrefl, K. Hono, Micromagnetic simulations on the grain size dependence of coercivity in anisotropic Nd–Fe–B sintered magnets, *Scripta Materialia*. 89 (2014) 29–32. <https://doi.org/10.1016/j.scriptamat.2014.06.020>.

- [18] S. Bance, B. Seebacher, T. Schrefl, L. Exl, M. Winklhofer, G. Hrkac, G. Zimanyi, T. Shoji, M. Yano, N. Sakuma, M. Ito, A. Kato, A. Manabe, Grain-size dependent demagnetizing factors in permanent magnets, *Journal of Applied Physics*. 116 (2014) 233903. <https://doi.org/10.1063/1.4904854>.
- [19] K. Hioki, High performance hot-deformed Nd-Fe-B magnets (Review), *Science and Technology of Advanced Materials*. 22 (2021) 72–84. <https://doi.org/10.1080/14686996.2020.1868049>.
- [20] W. Szmaja, Investigations of the domain structure of anisotropic sintered Nd-Fe-B-based permanent magnets, *Journal of Magnetism and Magnetic Materials*. 301 (2006) 546–561. <https://doi.org/10.1016/j.jmmm.2005.09.039>.
- [21] X. Tang, J. Li, Y. Miyazaki, H. Sepehri-Amin, T. Ohkubo, T. Schrefl, K. Hono, Relationship between the thermal stability of coercivity and the aspect ratio of grains in Nd-Fe-B magnets: Experimental and numerical approaches, *Acta Materialia*. 183 (2020) 408–417. <https://doi.org/10.1016/j.actamat.2019.11.038>.
- [22] M. Soderžnik, J. Li, L. Liu, H. Sepehri-Amin, T. Ohkubo, N. Sakuma, T. Shoji, A. Kato, T. Schrefl, K. Hono, Magnetization reversal process of anisotropic hot-deformed magnets observed by magneto-optical Kerr effect microscopy, *Journal of Alloys and Compounds*. 771 (2019) 51–59. <https://doi.org/10.1016/j.jallcom.2018.08.231>.
- [23] S. Sawatzki, T. Schneider, M. Yi, E. Bruder, S. Ener, M. Schönfeldt, K. Güth, B.-X. Xu, O. Gutfleisch, Anisotropic local hardening in hot-deformed Nd-Fe-B permanent magnets, *Acta Materialia*. 147 (2018) 176–183. <https://doi.org/10.1016/j.actamat.2017.12.059>.
- [24] L. Liu, H. Sepehri-Amin, T.T. Sasaki, T. Ohkubo, M. Yano, N. Sakuma, A. Kato, T. Shoji, K. Hono, Coercivity enhancement of Nd-Fe-B hot-deformed magnets by the eutectic grain boundary diffusion process using Nd-Ga-Cu and Nd-Fe-Ga-Cu alloys, *AIP Advances*. 8 (2018) 056205. <https://doi.org/10.1063/1.5006575>.
- [25] X. Xia, X. Tang, Y. Du, H. Wu, J. Ju, L. Wu, R. Chen, W. Yin, L. Zhang, A. Yan, Significant enhancement in the coercivity and thermal stability of bulk hot-deformed Nd-Fe-B magnets by intergranular addition of Nd-Dy/Tb-Cu-Ga alloys, *Acta Materialia*. 232 (2022) 117945. <https://doi.org/10.1016/j.actamat.2022.117945>.
- [26] I. Dirba, S. Sawatzki, O. Gutfleisch, Net-shape and crack-free production of Nd-Fe-B magnets by hot deformation, *Journal of Alloys and Compounds*. 589 (2014) 301–306. <https://doi.org/10.1016/j.jallcom.2013.11.188>.
- [27] Z.H. Kautsar, H. Sepehri-Amin, X. Tang, R. Iguchi, K. Uchida, T. Ohkubo, K. Hono, High-resistivity anisotropic hot-deformed Nd-Fe-B magnets prepared from DyF₃ electrophoretic deposited powders, *Journal of Alloys and Compounds*. 942 (2023) 168855. <https://doi.org/10.1016/j.jallcom.2023.168855>.
- [28] T. Zhang, S. Liu, Z. Wu, L. Zhang, R. Yu, Coercivity and remanence enhancement in hot-deformed Nd-Fe-B magnets by high-temperature short-term annealing process, *Journal of Alloys and Compounds*. 903 (2022) 163975. <https://doi.org/10.1016/j.jallcom.2022.163975>.
- [29] A. Bolyachkin, E. Dengina, N. Kulesh, X. Tang, H. Sepehri-Amin, T. Ohkubo, K. Hono, Tomography-based Digital Twin of Nd-Fe-B Permanent Magnets, (2023). [\[https://doi.org/10.21203/rs.3.rs-3281840/v1\]](https://doi.org/10.21203/rs.3.rs-3281840/v1)
- [30] J. Fischbacher, A. Kovacs, H. Oezelt, T. Schrefl, L. Exl, J. Fidler, D. Suess, N. Sakuma, M. Yano, A. Kato, T. Shoji, A. Manabe, Nonlinear conjugate gradient methods in micromagnetics, *AIP Advances*. 7 (2017) 045310. <https://doi.org/10.1063/1.4981902>.
- [31] J.M.D. Coey, *Magnetism and Magnetic Materials*, 1st ed., Cambridge University Press, 2001. <https://doi.org/10.1017/CBO9780511845000>.

- [32] H. Kronmüller, K.-D. Durst, S. Hock, G. Martinek, Micromagnetic analysis of the magnetic hardening mechanisms in RE-Fe-B magnets, *J. Phys. Colloques*. 49 (1988) C8-623-C8-628. <https://doi.org/10.1051/jphyscol:19888283>.
- [33] H. Kronmüller, D. Goll, I. Kleinschroth, A. Zern, Hysteresis Loops and Coercivity Mechanisms in Sintered and Nanocrystalline Permanent Magnets, *MRS Proc.* 577 (1999) 303. <https://doi.org/10.1557/PROC-577-303>.
- [34] J. Li, X. Tang, H. Sepehri-Amin, T. Ohkubo, K. Hioki, A. Hattori, K. Hono, On the temperature-dependent coercivities of anisotropic Nd-Fe-B magnet, *Acta Materialia*. 199 (2020) 288–296. <https://doi.org/10.1016/j.actamat.2020.08.040>.
- [35] Y. Murakami, T. Tanigaki, T.T. Sasaki, Y. Takeno, H.S. Park, T. Matsuda, T. Ohkubo, K. Hono, D. Shindo, Magnetism of ultrathin intergranular boundary regions in Nd–Fe–B permanent magnets, *Acta Materialia*. 71 (2014) 370–379. <https://doi.org/10.1016/j.actamat.2014.03.013>.
- [36] T. Kohashi, K. Motai, T. Nishiuchi, S. Hirosawa, Magnetism in grain-boundary phase of a NdFeB sintered magnet studied by spin-polarized scanning electron microscopy, *Applied Physics Letters*. 104 (2014) 232408. <https://doi.org/10.1063/1.4883487>.
- [37] T.T. Sasaki, T. Ohkubo, Y. Takada, T. Sato, A. Kato, Y. Kaneko, K. Hono, Formation of non-ferromagnetic grain boundary phase in a Ga-doped Nd-rich Nd–Fe–B sintered magnet, *Scripta Materialia*. 113 (2016) 218–221. <https://doi.org/10.1016/j.scriptamat.2015.10.042>.
- [38] A. Bolyachkin, E. Dengina, N. Kulesh, X. Tang, H. Sepehri-Amin, T. Ohkubo, K. Hono, Tomography-based Micromagnetic Simulations of Nd-Fe-B Hot-Deformed Magnets, in: *HMM 2023, Vienna, Austria, 2023*.
- [39] X. Tang, H. Sepehri-Amin, T. Ohkubo, K. Hono, Suppression of non-oriented grains in Nd-Fe-B hot-deformed magnets by Nb doping, *Scripta Materialia*. 147 (2018) 108–113. <https://doi.org/10.1016/j.scriptamat.2017.12.032>.
- [40] J. Fischbacher, A. Kovacs, L. Exl, J. Kühnel, E. Mehofer, H. Sepehri-Amin, T. Ohkubo, K. Hono, T. Schrefl, Searching the weakest link: Demagnetizing fields and magnetization reversal in permanent magnets, *Scripta Materialia*. 154 (2018) 253–258. <https://doi.org/10.1016/j.scriptamat.2017.11.020>.